



Cite this: *Nanoscale*, 2025, **17**, 12371

# Investigation of the phase transition to the Ruddlesden–Popper phase in La- or Nb-doped $\text{Sr}_2\text{Fe}_{1.5}\text{Mo}_{0.5}\text{O}_{6-\delta}$ double perovskites and the impact of lanthanum or niobium doping†

Agata Ducka,<sup>a</sup>  <sup>✉</sup> Patryk Błaszczak,<sup>a,b</sup> Marcin Zajac,<sup>c</sup> Alexey Maximenko,<sup>c</sup> Maria Gazda<sup>a</sup> and Beata Bochentyn<sup>a</sup>

$\text{Sr}_2\text{Fe}_{1.5}\text{Mo}_{0.5}\text{O}_{6-\delta}$  (SFM) is a well-known representative of the double perovskite family, recognized for its remarkable properties, such as good conductivity in air and hydrogen. However, this material can undergo a phase transition under reductive atmospheres, which might be a challenge for its practical use. Herein, we focus on the impact of lanthanum or niobium dopants, which would not only stabilize the structure during the reduction but also have a beneficial impact on the properties of the material, e.g., electrical conductivity. As a result, lanthanum doping (LSFM –  $\text{La}_{0.3}\text{Sr}_{1.7}\text{Fe}_{1.5}\text{Mo}_{0.5}\text{O}_{6-\delta}$ ) was found to be the most stable and the lowest amount of a new Ruddlesden–Popper phase was formed during the reduction. Moreover, the aliovalent La-doping resulted in increased electrical conductivities in both air and hydrogen compared to those of pristine SFM. Niobium doping resulted in a behavior similar to that of SFM with only slight stabilization, but the exsolution process in this material was found to be more intense. *In situ* studies during oxidation allowed us to retrieve the original structure at 700 °C. *Ex situ* XAS analyses enabled us to focus on the electronic state, which in most cases was restored almost to the original state after the re-oxidation process. This showed that not only the crystallographic structure but also the local atomic structure were re-established. The use of wavelet transform on the Fe K-edge allowed us to differentiate contributions from the Fe–Fe and Fe–Mo bonds in LSFM.

Received 10th February 2025,  
Accepted 29th March 2025

DOI: 10.1039/d5nr00596e

rsc.li/nanoscale

## 1. Introduction

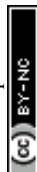
One of the challenges that the world faces today is the transition from fossil fuels to renewable energy sources. Additionally, hydrogen technologies are gaining more interest as a way to generate electricity or for energy storage. Among them, one may find solid oxide fuel cells (SOFCs), which can produce electricity from the chemical energy of the fuel. To make SOFCs even more advantageous, their ability to use fuels other than hydrogen should be developed. Unfortunately, the state-of-the-art anode material, Ni-YSZ cermet, performs poorly under other fuels and is prone to deactivation and carbon agglomeration. Thus, there is a need to develop novel anode

materials that would withstand such conditions. One of the candidates is perovskites with the general formula  $\text{ABO}_3$ , which offer a wide range of potential compounds with different properties.<sup>1</sup> In the perovskite family, double perovskites with the  $\text{A}_2\text{B}_2\text{O}_6$  formula can also be identified. Double perovskites can be present in A- or B-site ordered structures, resulting in formulas  $\text{AA}'\text{B}_2\text{O}_6$  or  $\text{A}_2\text{BB}'\text{O}_6$ , respectively. Moreover, different placements of A or B cations can lead to the formation of layered, columnar, or rock-salt ordered structures<sup>1</sup> with the last being the most common.<sup>2</sup>  $\text{Sr}_2\text{Fe}_{1.5}\text{Mo}_{0.5}\text{O}_{6-\delta}$  (SFM) is one of the representatives of the double perovskite sub-group, which exhibits good redox stability.<sup>2–7</sup> However, under highly reductive atmospheres, SFM compounds may undergo a phase transition to layered perovskites, more specifically the Ruddlesden–Popper (RP) phase  $\text{Sr}_3\text{Fe}_{1.5}\text{Mo}_{0.5}\text{O}_{7-\delta}$ .<sup>8–14</sup> The RP phase consists of at least one layer of  $\text{ABO}_3$  perovskite structure separated by AO rock-salt layers.<sup>10,15</sup> The higher-order Ruddlesden–Popper phases (more than 1 perovskite slab) are rich in oxygen vacancies in the perovskite layer.<sup>15</sup> Qiu *et al.*,<sup>13</sup> Lv *et al.*,<sup>12</sup> and Yang *et al.*<sup>11</sup> have shown that despite the formation of the Ruddlesden–Popper phase under a hydrogen atmosphere, SFM-based com-

<sup>a</sup>Faculty of Applied Physics and Mathematics, Gdansk University of Technology, ul. Narutowicza 11/12, 80-233 Gdańsk, Poland. E-mail: agata.ducka@pg.edu.pl

<sup>b</sup>Faculty of Electronics, Telecommunications and Informatics, Gdansk University of Technology, ul. Narutowicza 11/12, 80-233 Gdańsk, Poland

<sup>c</sup>National Synchrotron Radiation Centre SOLARIS, Jagiellonian University, Czerwone Maki 98, 30-392 Kraków, Poland

†Electronic supplementary information (ESI) available. See DOI: <https://doi.org/10.1039/d5nr00596e>


pounds transform back to double perovskites after the re-oxidation process. In addition to inconsistency with respect to redox stability, SFM is also characterized by high conductivity in air and hydrogen, making it an interesting candidate for electrodes in sSOFCs (symmetrical solid oxide fuel cells).<sup>4,5,16–19</sup> Although studies agree that the electrical conductivity of SFM is high, the values reported in the literature vary significantly. Liu *et al.*<sup>18</sup> have obtained extraordinarily high conductivities of 310 S cm<sup>−1</sup> and 550 S cm<sup>−1</sup> at 780 °C in hydrogen and air, respectively. Furthermore, Li *et al.*<sup>3</sup> have reported a high conductivity of 116 S cm<sup>−1</sup> in air. Although these results are undoubtedly impressive, they remain a minority. Most studies<sup>5,17,20–22</sup> present conductivities in the range of 10–50 S cm<sup>−1</sup> under both the mentioned atmospheres and in CO/CO<sub>2</sub> mixtures.

Generally, doping is a standard method for enhancing the properties of any perovskites. Many studies are devoted to transition metal doping at the B-site to enhance the catalytic properties of SFM.<sup>6,12,23–25</sup> Furthermore, electrical conductivity could be increased simultaneously by doping of Ca<sup>2+</sup>, Ba<sup>2+</sup>, or La<sup>3+</sup> at the Sr site.<sup>6,15,23,24,26</sup>

This work focuses on the doping of SFM with La<sup>3+</sup> (at the A-site) or Nb<sup>5+</sup> (at the B-site). In a similar system, Nb-doping for the Mo-site was studied and it revealed that more oxygen vacancies were formed upon doping.<sup>25</sup> Gou *et al.*<sup>5</sup> suggested that Nb<sup>5+</sup> may increase the stability of SFM-based compounds. In their work, they have also shown that Nb-doping improves the electrical conductivity in both air and hydrogen, and finally increases the power density of a symmetrical cell at 800 °C from 374.1 mW cm<sup>−2</sup> to 531.5 mW cm<sup>−2</sup>. Yang *et al.*<sup>6</sup> examined the influence of La-doping and it was shown that moderate doping enhanced electrical conductivity, but on the other hand, excess La resulted in a decrease in conductivity. Such behavior was explained by an increase in the concentration of anti-site defects and electron density at the Fermi level. Herein, we present a study of the properties of La- or Nb-doped SFM. The impact of the dopant on the phase stability in hydrogen was addressed and extensively studied using various techniques, *i.e.*, high-temperature XRD (X-ray diffraction), DSC/TG (differential scanning calorimetry/thermogravimetry), and several XAS (X-ray absorption spectroscopy) measurements. Moreover, the reversible nature of the phase transition was investigated. After the reduction in hydrogen, the exsolution process was observed.

## 2. Experimental

### 2.1. Synthesis

The chemical formulas of the prepared materials are as follows: Sr<sub>2</sub>Fe<sub>1.5</sub>Mo<sub>0.5</sub>O<sub>6−δ</sub> (SFM), La<sub>0.3</sub>Sr<sub>1.7</sub>Fe<sub>1.5</sub>Mo<sub>0.5</sub>O<sub>6−δ</sub> (LSFM), and Sr<sub>2</sub>Fe<sub>1.425</sub>Mo<sub>0.475</sub>Nb<sub>0.1</sub>O<sub>6−δ</sub> (SFMNb). All compounds were synthesized by a modified Pechini method. Appropriate amounts of salts (Fe(NO<sub>3</sub>)<sub>3</sub>·9H<sub>2</sub>O, Sr(NO<sub>3</sub>)<sub>2</sub>, and (NH<sub>4</sub>)<sub>6</sub>Mo<sub>7</sub>O<sub>24</sub>·4H<sub>2</sub>O) were dissolved in deionized water at room temperature. For doped samples, La(NO<sub>3</sub>)<sub>3</sub>·9H<sub>2</sub>O and

NbCl<sub>5</sub> were used as the sources of lanthanum and niobium, respectively. Then citric acid and ethylene glycol were added to the beakers. All reagents used for the synthesis were of analytical grade. The solutions obtained were stirred and gradually heated to 200 °C until gels formed. The gels obtained were transferred to alumina crucibles and fired at 1100 °C for 10 h. The heating and cooling rates were 3 °C min<sup>−1</sup>. To analyze the stability of the material under the reductive atmosphere and to perform exsolution, finely ground powders were placed in the tube furnace and reduced under a hydrogen flow for 4 h at 800 °C. The part of the reduced powders was re-oxidized in air for 4 h at 800 °C to analyze the reversibility of the phase transition.

### 2.2. Characterization methods

To determine the phase composition of the materials, X-ray diffraction (XRD) measurements were performed using a Bruker D2 PHASER XE-T. XRD patterns were recorded mainly at room temperature, unless otherwise indicated. High-temperature XRD measurements under air atmosphere were performed using a Philipps X'Pert Pro diffractometer with a high-temperature Anthon Paar HT-1200 oven adapter. Both diffractometers were equipped with Cu-Kα radiation sources. To analyze the obtained diffraction patterns, HighScore Plus 3.0.2 software from PANalytical was used.

The microstructure and morphology of the investigated materials were studied using a scanning electron microscope (FEI Quanta FEG 250) with a secondary electron detector operating in high vacuum mode with an acceleration voltage of 10 kV.

Simultaneous thermogravimetry (TG) and differential scanning calorimetry (DSC) measurements were performed under synthetic air using a Netzsch STA 449 F1 Jupiter apparatus. Data were collected from room temperature to 900 °C at a heating rate of 5 °C min<sup>−1</sup>. For each analysis, around 10 mg of a powder with a ±10% tolerance factor was used.

X-ray absorption spectroscopy (XAS) measurements were performed at the SOLARIS National Synchrotron Radiation Center in Kraków (Poland) at the PIRX and ASTRA beamlines. For the measurements of the O K-edges and Fe L<sub>3,2</sub>-edges, well-ground powders were evenly distributed on carbon tape and then placed on a standard flag-style sample holder. The measurements were performed at room temperature under ultra-high vacuum in total electron yield (TEY) mode at the PIRX beamline. The Fe K- and Mo L<sub>3</sub>-edges were obtained at the ASTRA beamline. The spectra were recorded using a photon beam delivered using a double-bend achromatic 1.3 T bending magnet with a critical energy of around 2 keV. For the K-edge of the iron, an appropriate amount of the finely ground powder was mixed with ethylcellulose (50 μm, Pol-Aura) and pressed into thin pellets. The Fe K-edges were obtained at room temperature under ambient pressure and a Ge (220) monochromator was used. At the same time, Fe foil was used each time as a reference. To measure the Mo L<sub>3</sub>-edge, the powders were evenly distributed on a sulfur-free Kapton foil and measured at around 30 Torr. The MoO<sub>3</sub> spectrum was



recorded every two samples as a reference material and the Si (111) crystal was used as a monochromator. Data were analyzed using the freeware Demeter package. For Fourier transform EXAFS analysis, the wave vector  $k$  was considered in the range of 2.9–8.5 Å<sup>-1</sup> and phase correction was applied. Because of the complex structure and the overlap of the Fe–Fe and Fe–Mo bonds in the radial distribution function, wavelet analysis was performed to differentiate between them. Wavelet analysis was performed using Fastosh freeware software. For the analysis,  $\eta = 7.5$  and  $\sigma = 0.5$  were used as parameters for the Morlet wavelet transform.

The conductivity of the compounds was measured using the direct current 4-wire method (DC4W). For this purpose, the samples were pressed into square pellets and sintered at 1400 °C for 10 h for densification. Subsequently, dense (>95% relative density) pellets were cut into narrow, rectangular bars, onto which platinum paste (ESL) was brush-painted and Pt wires were attached. For the measurements, a Keithley 2401 current source was used, while the voltage was measured using a Keysight 34970A meter. Each sample was first heated to 800 °C in air and then conductivity measurements were performed every 50 °C during cooling to 300 °C. After each temperature change, the samples were stabilized for the required amount of time. Before the atmosphere was changed to hydrogen, the cell was rinsed with Ar until no air remained inside and then the procedure was repeated in hydrogen. The only difference was that the samples were kept at 800 °C for 4 hours to mimic the reduction process.

### 3. Results and discussion

#### 3.1. Phase composition and structure of the materials

The diffraction studies revealed that all synthesized compounds were double perovskites in the  $Fm\bar{3}m$  structure, as presented in the XRD diffraction patterns in Fig. 1. For the doped compounds, a small amount of SrMoO<sub>4</sub> can be found; however, based on the Rietveld refinement, it was estimated that the samples contained less than 2 wt% Mo-rich impurities. The presence of SrMoO<sub>4</sub> in the as-prepared compounds is commonly reported in the literature<sup>18,25,27–31</sup> and tends to vanish after reduction. The detailed results of the Rietveld refinement are given in Table 1, while the exemplary results of refinement are presented in Fig. S1 in the ESI.† Both the doped materials have a unit cell larger than that of a pristine strontium ferrite. Although La<sup>3+</sup> has a smaller ionic radius than Sr<sup>2+</sup>, aliovalent doping may lead to changes in the valence state of Fe or Mo to preserve the electroneutrality of the compound. Both Fe and Mo, when in lower oxidation states, have larger ionic radii than their higher valence counterparts,<sup>27</sup> leading to the expansion of the unit cell.<sup>28</sup> Yang *et al.*<sup>6</sup> also explained the expansion of the unit cell upon La-doping by the domination of the electronic effect of La<sup>3+</sup> over the ionic size. They proposed that an additional electron from La<sup>3+</sup> influences primarily the Mo valence state, with only little impact on the Fe state.<sup>6</sup> The expansion of the unit cell in

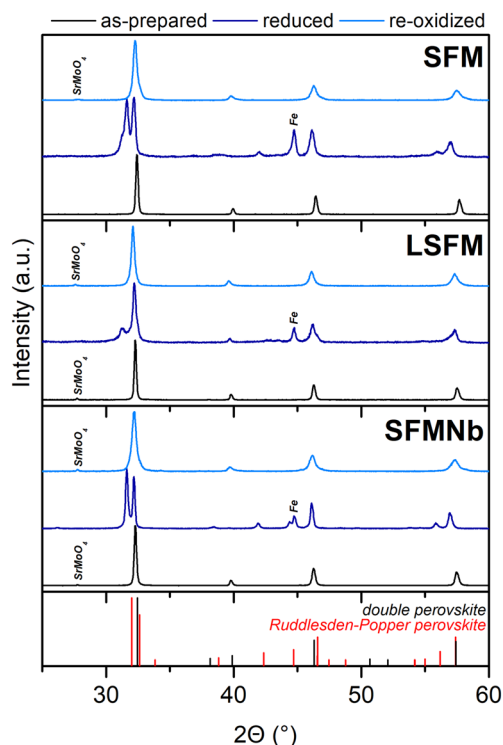


Fig. 1 XRD patterns of pristine and La- and Nb-doped SFM in three different states: as-prepared, reduced, and re-oxidized.

the SFMNb material can be directly explained by the size effect. Because niobium is a transition metal close to Mo in the periodic table, it is almost certain that it will incorporate into the B-site of the double perovskite, as was aimed during the synthesis. Furthermore, the size of Nb<sup>5+</sup> ions is quite similar to those of Fe and Mo ones, and almost twice smaller than that of Sr<sup>2+</sup> ions, and thus it was assumed that Nb occupies only the B-site of the double perovskite. Nb<sup>5+</sup> cations have an ionic radius equal to 0.64 Å, which is greater than for both possible molybdenum ions (Mo<sup>5+</sup> 0.61 Å and Mo<sup>6+</sup> 0.59 Å). At the same time, the ionic radius of Nb is slightly smaller than that of Fe<sup>3+</sup> (0.645 Å) and much smaller than that of Fe<sup>2+</sup> (0.78 Å).<sup>27</sup> According to ref. 5, niobium doping may result in the formation of a higher share of Fe<sup>2+</sup>, which would lead to cell enlargement.

As evidenced by the formation of a diffraction reflection at ~31°, after the reduction at 800 °C, a phase transition to the layered perovskite occurred. On the basis of the intensity ratio of the two components of the double reflection around 31–32°, it can be said that the transition is not complete and some double perovskite residuals remain in the materials. Because the reflection characteristic of the layered perovskite has a rather low intensity in the La-doped perovskite, it was suggested that lanthanum doping may stabilize the structure and restrict the phase transition. Phase composition was calculated from Rietveld refinement and fitting the double perovskite structure (Sr<sub>2</sub>Fe<sub>1.5</sub>Mo<sub>0.5</sub>O<sub>6-δ</sub>- $Fm\bar{3}m$ ), the oxygen-deficient Ruddlesden–Popper layered perovskite



**Table 1** Results of the Rietveld refinement for the pristine and La- and Nb-doped SFM compounds

			SFM	LSFM	SFMNb
As-prepared	Double perovskite ( $Fm\bar{3}m$ )	$a = b = c$ (Å)	7.8411(2)	7.8533(2)	7.8632(2)
		$V$ (Å <sup>3</sup> )	482.09	484.34	486.18
		SrMoO <sub>4</sub> amount (wt%)	n/a	1.7	0.8
		GOF	1.53	1.47	1.65
Reduced	Double perovskite ( $Fm\bar{3}m$ )	$a = b = c$ (Å)	7.854(2)	7.884(1)	7.896(1)
		$V$ (Å <sup>3</sup> )	484.49	490.05	492.29
		Amount (wt%)	17.7	52.2	7.6
		GOF	1.53	1.47	1.65
	Ruddlesden–Popper layered perovskite ( $I4/mmm$ )	$a = b$ (Å)	3.9348(6)	3.933(1)	3.9436(2)
		$c$ (Å)	20.361(4)	20.951(9)	20.435(1)
		$V$ (Å <sup>3</sup> )	315.24	324.08	317.81
		Amount (wt%)	73.2	39.2	79.1
		Iron amount (wt%)	9.1	8.6	13.3
		GOF	2.69	1.67	2.21
As-prepared	Double perovskite ( $Fm\bar{3}m$ )	$a = b = c$ (Å)	7.8516(6)	7.8538(3)	7.8771(6)
		$V$ (Å <sup>3</sup> )	484.03	484.44	488.76
		Amount of SrMoO <sub>4</sub> (wt%)	1.2	1.7	1.2
		GOF	1.87	1.55	1.83

(Sr<sub>3</sub>Fe<sub>1.5</sub>Mo<sub>0.5</sub>O<sub>7-δ</sub>-*I4/mmm*) and iron (*Im* $\bar{1}m$ ), which can be exsolved from the lattice. The results of the refinement are presented in Table 1. For both the pristine and Nb-doped samples, the content of the newly formed layered perovskite is between 70 and 80 wt%, while for LSFM, this amount is about 40 wt%. Although the presence of the Ruddlesden–Popper phase may be beneficial and enhance the exsolution of catalytically active centers,<sup>12,13,29</sup> it also presents several challenges that need to be addressed. As seen in Table 1, the double perovskite has a larger unit cell volume compared to the Ruddlesden–Popper phase. Therefore, during reduction, this volume change would introduce significant strain. For potential use as an electrode in SOCs, this may lead to delamination of the electrode and decrease in the TPB (triple phase boundary). Several studies claim that pristine SFM should be redox stable at high temperatures and not susceptible to exsolution phenomena;<sup>3,12,18</sup> however, the XRD patterns of the reduced samples revealed the formation of metallic iron. A similar observation was made by Qiu *et al.*<sup>13</sup> for Co-doped SFM. Interestingly, the amount of exsolved iron was the highest (~13 wt%) for the SFMNb sample, suggesting that Nb-doping at the B-site enhanced the exsolution of iron. Although the segregation energy of Fe (0.91 eV) makes it unfavorable for exsolution, the addition of other transition metals would introduce cation defects and/or oxygen vacancies.<sup>12</sup> As a result, the segregation energy will be lowered, promoting the formation of nanoparticles.

The reversibility of the phase transition was studied after re-oxidizing the materials at 800 °C for 4 h. All compounds were transformed back to their original double perovskite structure without traces of the layered perovskite. Also, in all XRD patterns, SrMoO<sub>4</sub> was found, even for SFM, which was free of this impurity before reduction. Although the structure was successfully restored, the unit cell was larger than that of the as-prepared samples. This relates mostly to the pristine and Nb-doped samples, while the La-doped one is characterized by only a slight volume expansion.

SEM images of the as-prepared materials are presented in Fig. S2 in the ESI.† In the case of the pristine SFM and SFMNb compounds, the grains' boundaries are obliterated and difficult to spot. On the other hand, La-doping resulted in the formation of well-defined, round-shaped grains. The microstructures of the reduced powders are presented in Fig. 2. Interestingly, the microstructure of the undoped sample seems denser than before the reduction. Although the grains' boundaries are still quite blurred, areas consisting of smaller grains of a rectangular shape along the original round grains may be noticed. The existence of the rectangular shape originates from the transition to a layered perovskite. Some nanoparticles were found; however, their number is rather low. A similar number of nanoparticles with diameter <100 nm was observed for LSFM. The highest concentration of the exsolved NPs was observed for the Nb-doped material, which was expected in the XRD studies, showing the highest Fe content. The NPs have a round shape and their diameter is smaller than 100 nm. Enhancement of the exsolution phenomena, thanks to Nb-doping, may result from a lower valence state of Fe ions in the as-prepared compound. Such an observation was reported by Gou *et al.*<sup>5</sup> for a similar material. As a result, iron from the lattice is easier to reduce on the surface, forming visible nanoparticles. Here, based on ref. 12, in which TEM-EDS did not find any molybdenum in the exsolved NPs, it was stated that the formed NPs were composed of metallic Fe, if no other easily reduced transition metal is introduced into the B-site lattice. Although niobium is also a transition metal, its reduction requires much higher temperatures than those used in this experiment.<sup>5,30</sup>

The structures of the re-oxidized compounds are presented in Fig. S2.† The exsolved nanoparticles are not visible anymore after the oxidation and the microstructure looks a lot like that of the as-prepared materials. Such an observation indicates the reversibility of the phase transition followed by dissolution of the exsolved NPs. Moreover, it is possible to retrieve not only





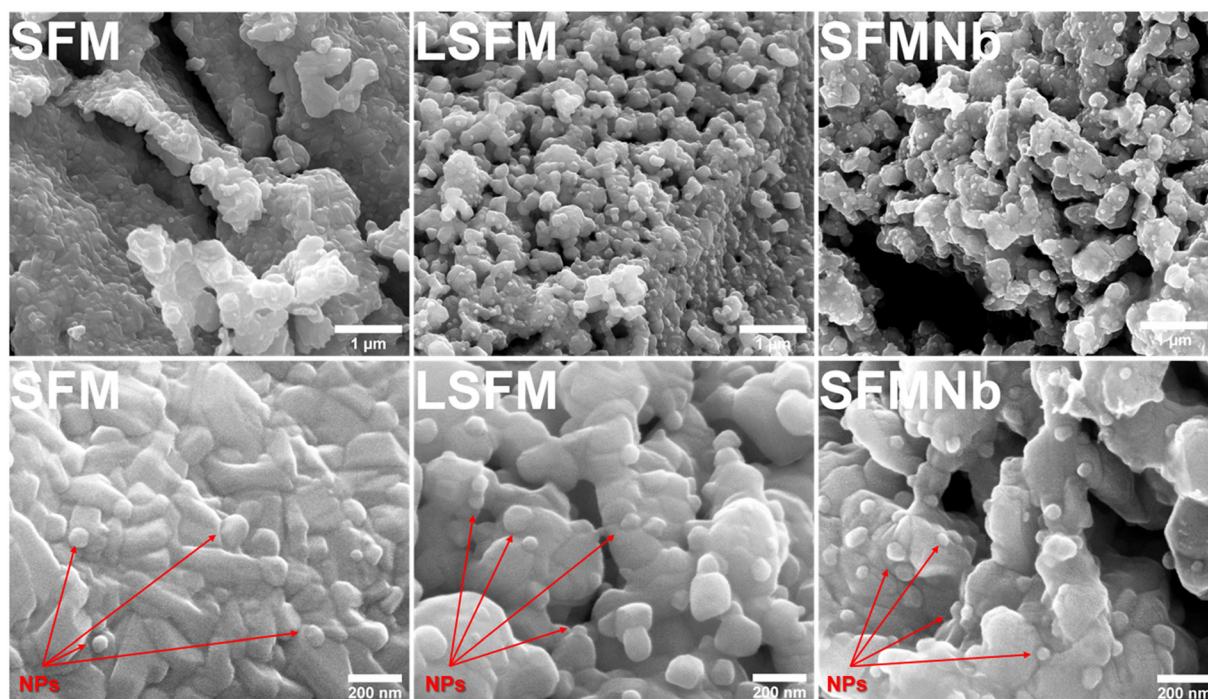


Fig. 2 SEM images of the powders reduced at 800 °C in hydrogen.

the specific crystal structure but also the microstructure of the compounds.

### 3.2. *In situ* oxidation studies from the Ruddlesden–Popper perovskite to the double perovskite

As the phase transition was demonstrated to be reversible by *ex situ* XRD analyses, HT-XRD measurements were performed to investigate the process of shifting from the layered perovskite to the double perovskite in air. The diffractograms

obtained during heating are presented in Fig. S3 in the ESI.† Fig. 3 presents the heat maps of the normalized intensities of the main XRD reflections corresponding to the Ruddlesden–Popper and double perovskite phases *vs.* temperature. For the pristine and SFMNb samples, the intensities of both reflections between room temperature and approximately 600 °C are comparable, resulting in the highest amount of the RP perovskite. On the other hand, in the case of LSFM, the amount of the RP phase is smaller. As a result, the diffraction peak at

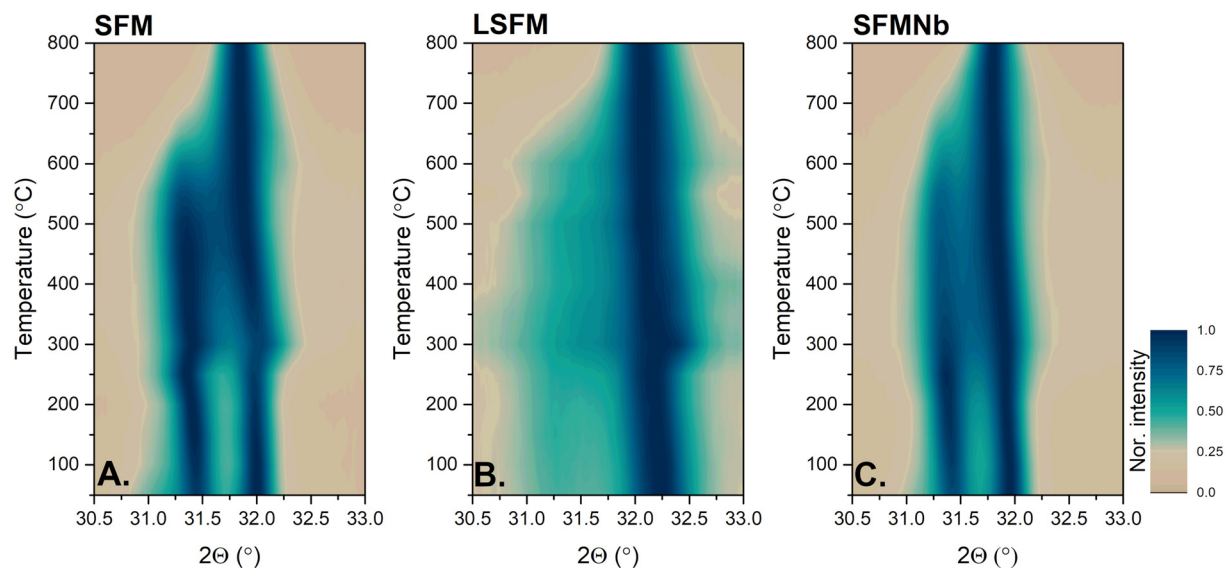


Fig. 3 Heatmaps of the normalized main peak from the reduced samples obtained from *in situ* oxidation studies.



$\sim 31^\circ$  is less intense and is visible as a halo between  $31$  and  $31.5^\circ$ . For all compounds, the reflections shifted towards lower  $2\theta$ , as the unit cells gradually expanded with increasing temperature. At  $250^\circ\text{C}$ , the shift toward higher angles is visible in all three samples, being the most intense for the pristine and La-doped SFM samples. The features seen at around  $250^\circ\text{C}$  in Fig. 3 are accompanied by a vanishing signal from iron observed at the same temperature (Fig. S4†). This could originate from iron dissolving back into the perovskite and the beginning of oxidation to the double perovskite. As the temperature was further increased, the main reflections are getting closer to each other, which originates from a decrease in the  $c$ -parameter of the Ruddlesden–Popper phase. The peak characteristic of the Ruddlesden–Popper phase vanished between  $600^\circ\text{C}$  and  $700^\circ\text{C}$ .

To further analyze the phase transition, DSC/TG measurements were performed on the pre-reduced powders. The results are shown in Fig. 4. The first process, clearly seen on the TG curve up to  $200^\circ\text{C}$ , results from the release of adsorbed water. Furthermore, a slower decrease in the mass (between  $200$  and  $300^\circ\text{C}$ ) may be due to the loss of structural water. With a further increase in the temperature, the mass above  $300^\circ\text{C}$  increases at a higher rate for SFM and SFMNb, while for LSFM, the process is more gradual. In addition, the increase in the TG signal correlates with an exothermic DSC peak, which originates from the oxidation of iron. The temperature of the process corresponds well with the vanishing of the iron peak in HT-XRD (Fig. S4†). Furthermore, the intensity of the DSC peak is the highest for the SFMNb sample, which was characterized by the highest amount of exsolved Fe nanoparticles, observed in both XRD and SEM analyses. In the DSC signal, no other clearly distinguishable peaks were found. However, the TG signal shows a gradual loss of mass, except

for the LSFM sample, in the  $350$ – $650^\circ\text{C}$  range, which perfectly fits the phase transition regime visible in HT-XRD. The mass decreases above  $700^\circ\text{C}$  ( $750^\circ\text{C}$  for LSFM), which is likely the result of the release of surplus oxygen from the Ruddlesden–Popper phase. The combined mass loss at  $750^\circ\text{C}$  and the formation of a single peak in HT-XRD are indicators of complete phase transition to the double perovskite.

### 3.3. Ex situ X-ray absorption studies

The O K-edge spectra obtained for pristine and La- and Nb-doped SFM in three different states are presented in Fig. 5A–C. The peaks visible in the spectra can be assigned to the respective excitation of O 1s to the hybridized Fe 3d–O 2p ( $\sim 530$  eV), followed by Sr 4d–O 2p ( $\sim 536$  eV) and Fe 4sp–O 2p ( $\sim 543$  eV).<sup>31–33</sup> Iron in the perovskites is predominantly present in the  $3d^5$  ground state. Abbate *et al.*<sup>32</sup> have studied the ground states in both  $\text{SrFeO}_3$  and  $\text{LaFeO}_3$ . They concluded that in  $\text{SrFeO}_3$ , iron is found in the  $3d^5\text{L}$  ( $\text{Fe}^{4+}$ ) state, where L stands for the presence of ligand holes, while for  $\text{LaFeO}_3$ , the ground state of iron is  $3d^5$  ( $\text{Fe}^{3+}$ ). Here, the presence of the  $\text{Fe}^{4+} 3d^5\text{L}$  state can be recognized by the pre-peak feature at  $\sim 528$  eV, which is most intense for re-oxidized SFM and LSFM. The as-prepared samples are also characterized by this feature, but with a lower intensity. The main peak visible in all spectra of the prepared sample originating from the  $t_{2g}$  orbital is slightly shifted to lower energies when compared to the signal of  $\text{Fe}^{3+}$  oxides, also the presence of  $\text{Fe}^{4+}$  in these states.<sup>32,34</sup> On the other hand, the signal from higher  $e_g$  orbitals is visible only as a small bump at around  $534$  eV. Xi *et al.*<sup>35</sup> have explained the enhanced formation of the  $e_g$  orbitals by structural deformation. The formation of the  $t_{2g}$  and  $e_g$  peaks originates from crystal field splitting around the transition metal sites.<sup>33,35</sup>

After the reduction, significant changes are visible in the spectra of all compounds. First, the peak labeled as  $t_{2g}$  is shifted to higher energies and split into a doublet. The change originates from the reduction of  $\text{Fe}^{4+}$  to  $\text{Fe}^{3+}$  and follows the trend reported by Abbate *et al.*<sup>32</sup> Simultaneously, the formation of a doublet arises from the splitting of  $t_{2g}$  into  $d_{xz}$ ,  $d_{yz}$  and  $d_{xy}$  orbitals, respectively, due to the distortion of the unit cell or the formation of oxygen vacancies.<sup>35,36</sup> At the same time, crystal field splitting occurs for the  $e_g$  orbitals as well, which split into the  $d_{z^2}$  and  $d_{x^2-y^2}$  orbitals, respectively. These observations are in line with the formation of a more complex structure of the Ruddlesden–Popper layered perovskite. The splitting is the most intense for the  $e_g$  orbital of SFMNb. Moreover, exceptionally this sample gave a different spectrum after the re-oxidation. The  $t_{2g}$  peak is shifted to higher energies, while  $e_g$  peak is significantly less intense. Moreover, the peak originating from Sr 4d–O 2p is shifted to higher energies. It is unlike all other samples in which the aforementioned peak remains almost unaffected in terms of energy regime. This observation is particularly interesting because no significant changes have been observed during XRD measurements, both *ex situ* and *in situ* high-temperature measurements. The differences in the spectra of SFMNb may originate from electron transfer between the Fe–Nb and Mo–Nb orbitals.

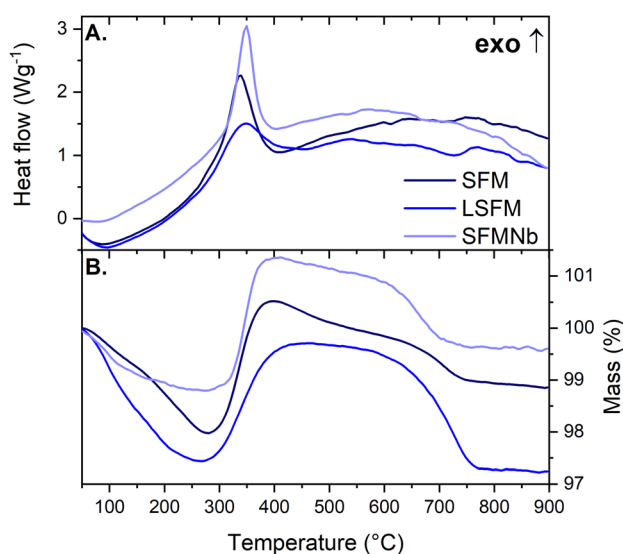
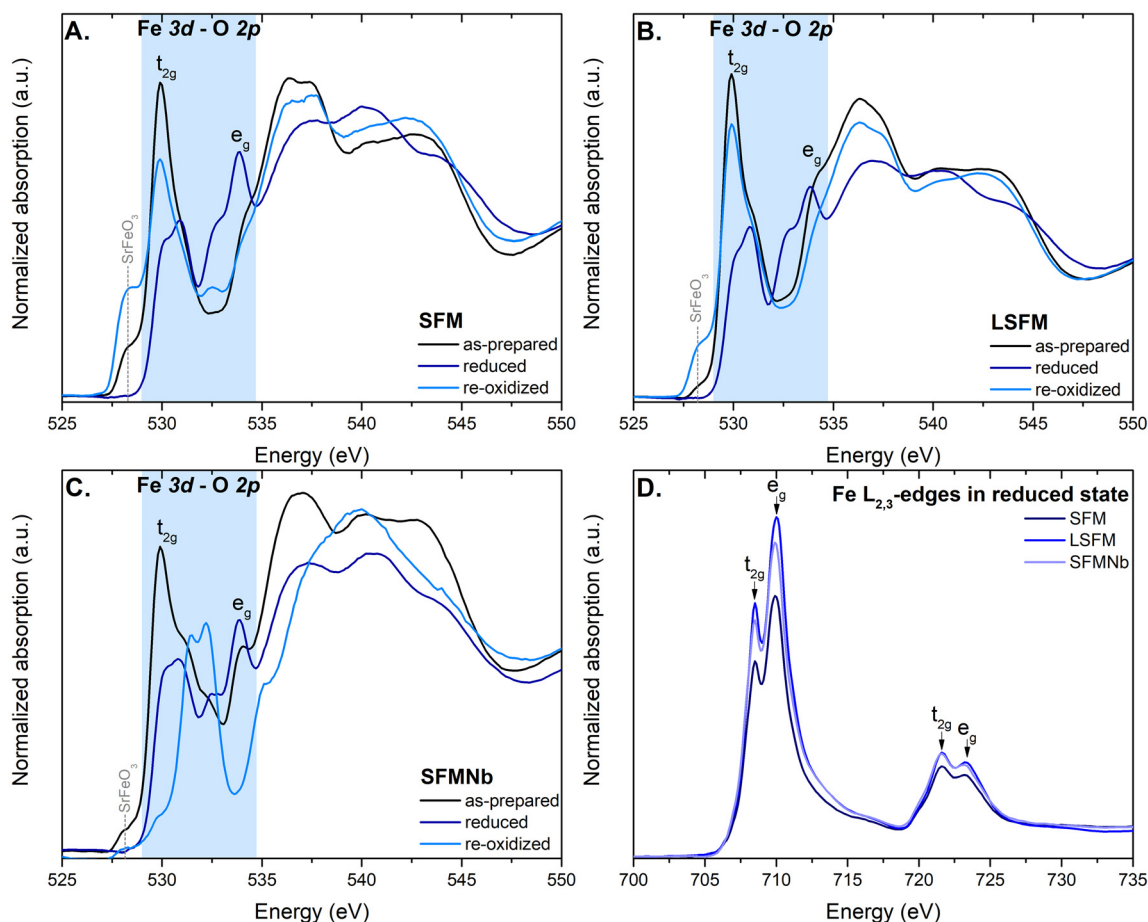


Fig. 4 Simultaneous thermal analyses for the re-oxidation of the pristine and La-, and Nb-doped SFM compounds: (A) DSC and (B) TG.





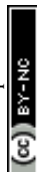
**Fig. 5** Normalized X-ray absorption edges obtained for the compounds in different states (as-prepared, reduced, and re-oxidized): (A) O K-edge of SFM, (B) O K-edge of LSFM, (C) O K-edge of SFMNb, and (D) Fe  $L_{2,3}$ -edge in the reduced state only of all three materials.

Fig. 5D shows the Fe- $L_{2,3}$  edges of the SFM-based compounds after reduction in  $H_2$ . The obtained spectra are typical of  $Fe^{3+}$  in octahedral coordination.<sup>32,37–39</sup> According to ref. 32, such spectra originate from a high spin  $t_{2g}^3 e_g^2$  ground state of  $3d^5$  and the  $10Dq$  value was calculated to be 1.6 eV. The value was calculated based on the minima of the second derivative of the  $L_3$ -edge. The exemplary spectrum with its derivative is shown in Fig. S5.† However, the spectra are characterized by a similar shape originating from the  $Fe^{3+}$  cations, and the intensities of the white lines are different. The intensity of the L-edge carries information about the unoccupied d-orbitals and may suggest a higher valence of the element.<sup>40</sup> In this case, in SFM, more  $Fe^{2+}$  ions are formed after reduction compared to both doped materials. The spectra of the as-prepared and re-oxidized compounds are presented in Fig. S6 in the ESI.† Regardless of the reduction, the ground state of Fe remained unaffected and iron was found to be present mainly as  $Fe^{3+}$  cations.

The use of hard X-rays allowed for probing the K-edge of iron in the compounds of interest. Normalized XANES spectra of SFM, LSFM, and SFMNb are presented in Fig. 6A–C. As expected, based on the  $L_{2,3}$ -edges, the K-edge spectra are

characteristic of  $Fe^{3+}$  in the octahedral coordination of the perovskite.<sup>35</sup> A comparison of the K-edge spectra of the as-prepared SFM and references is presented in Fig. S7 in the ESI.† Although the spectra are of an overall similar shape, some significant differences can be spotted. First, the pre-edge feature originating from the presence of hybridized 3d–4p orbitals and two contributions originating from the dipole transition  $1s \rightarrow 4p$  and quadrupole transition  $1s \rightarrow 3d$ .<sup>41,42</sup> Hybridization of 3d–4p would not occur in ideal octahedral structures; thus, distortion must be present in SFM-based materials.<sup>42</sup>

However, the reduction does not affect the shape of the K-edge and it has an impact on the intensity of the white line. The decrease in white-line intensity is the most visible for doped SFM, suggesting a partial reduction to iron ions as visible in SEM imaging. At the same time, the pre-edge feature was enhanced for the undoped sample. In general, all the analyzed samples have the lowest white line intensity for the reduced samples. This observation coupled with a slight shift of the pre-edge suggests partial reduction to  $Fe^{2+}$  ions. After the re-oxidation process, the white line intensity increased almost returns back to the original. In the case of both the doped SFM-based compounds, the edge was higher, most





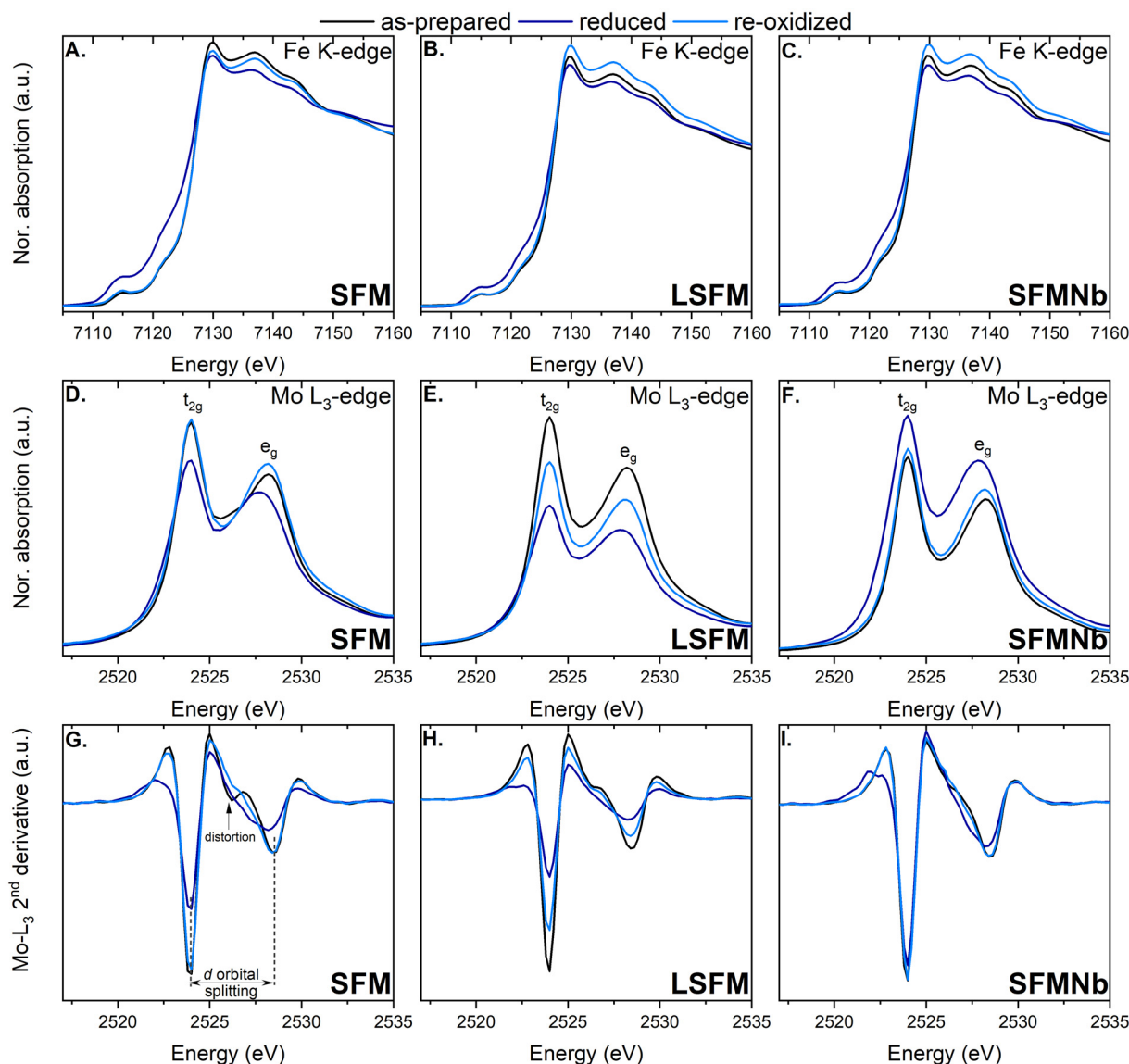


**Fig. 6** Normalized Fe K-edges for SFM (A), LSFM (B), and SFMNb (C); normalized Mo  $L_3$ -edges for SFM (D), LSFM (E), and SFMNb (F); and 2<sup>nd</sup> derivatives of Mo- $L_3$  edges for SFM (G), LSFM (H), and SFMNb (I).

probably because of the changes in the density of states (DOS). The higher the white line, the lower the DOS.

The  $L_3$ -edges of molybdenum were also measured and the normalized spectra are presented in Fig. 6D–F. Based solely on the intensity of the peaks (ratio 3 : 2), it is easy to confirm that molybdenum is also present in octahedral coordination.<sup>43,44</sup> The first peak at ~2523 eV originates from excitation to the  $t_{2g}$  states and the latter peak at ~2527 eV appears due to the transition to  $e_g$  state.<sup>25</sup> Based on the study by Vasala *et al.*,<sup>25</sup> in the as-prepared samples, both the aforementioned states should be empty and the reduction would introduce electrons into the  $t_{2g}$  state. As a result, the peak from the reduced samples should be lower than in the as-prepared one. Such an observation is made for the pristine SFM and La-doped samples. Interestingly, the behavior for SFMNb is different, which could

originate from electron transfer between the Mo and Nb cations. Based on the  $L_3$  spectra, it may be deduced that molybdenum has been partially reduced to  $Mo^{5+}$  during reduction, which can be determined by occupation of the  $t_{2g}$  and  $e_g$  states. Another indication of octahedral geometry is the value of d-orbital splitting, which was calculated as a difference between two minima in the second derivative of the respective compounds.<sup>44</sup> The second derivatives of the Mo  $L_3$ -edge spectra are presented in Fig. 6G–I. The aforementioned splitting was found to be in the range of 4.2 eV–4.4 eV, typical of the octahedral structure<sup>43,45</sup> and slightly smaller than those obtained for the Mo-based double perovskites.<sup>46</sup>

The Fourier transform EXAFS spectra of the respective compounds are presented in Fig. 7. Due to the complicated nature of the compounds, only qualitative analysis was performed.





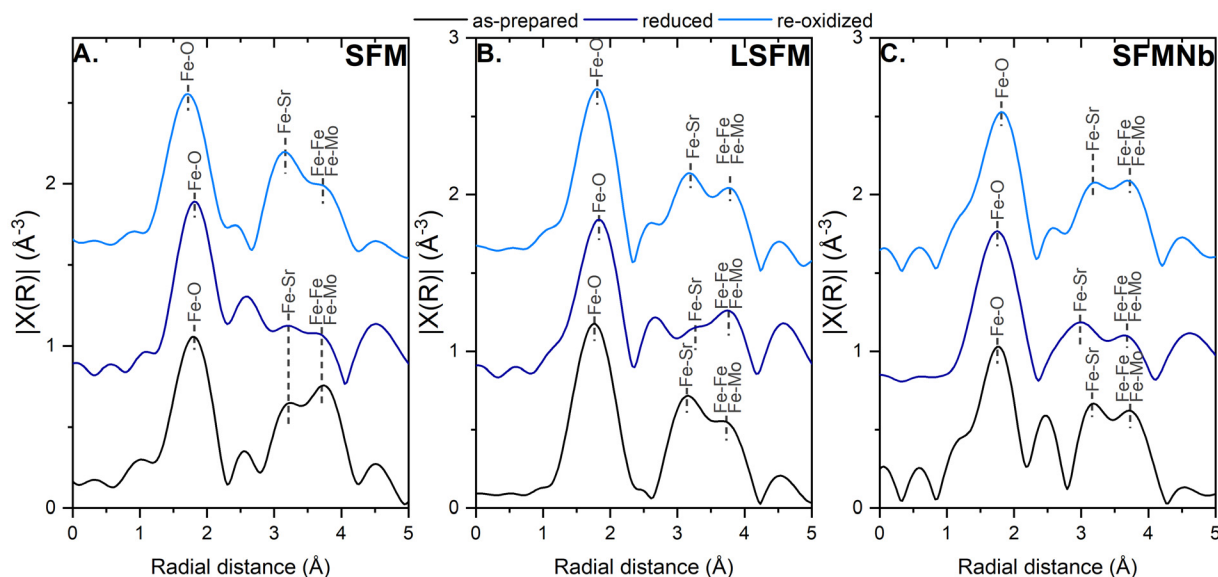


Fig. 7 Fourier transform of the Fe K-edge EXAFS for (A) SFM, (B) LSM, and (C) SFMNb.

The main peak visible at  $\sim 1.75$  Å in all cases originates from the Fe–O bond. The position of the Fe–O peak corresponds well with the expected bond length from the crystal structures of the prepared compounds. In the reduced compounds, the peak is slightly shifted to higher values, which is characteristic of the Ruddlesden–Popper layered perovskite. The re-oxidized materials are characterized by similar bond lengths compared to their as-prepared counterparts, which shows that the structure has been restored to its original state. The next characteristic peak originates from the Fe–Sr bond, which tends to be slightly shorter after the reduction as a result of the formation of the RP phase. Exceptionally for LSM, this scattering path

was elongated, which originates from the expansion of the original unit cell during the reduction. The Fe–Sr peak is followed by the peak coming from the single-scattering path on the Fe–Fe/Mo bonds. In the case of Nb-doping, the signal originating from the Fe–Nb scattering pathway would overlap with other Fe–Fe and Fe–Mo paths. As both Fe and Mo occupy equivalent positions, it is impossible to differentiate each contribution to the scattering pathways.

As mentioned above, the scattering paths from the Fe–Fe and Fe–Mo bonds overlap in the Fourier transform EXAFS spectra, making it impossible to differentiate between them. Thus, the analysis was extended to wavelet transform to reveal

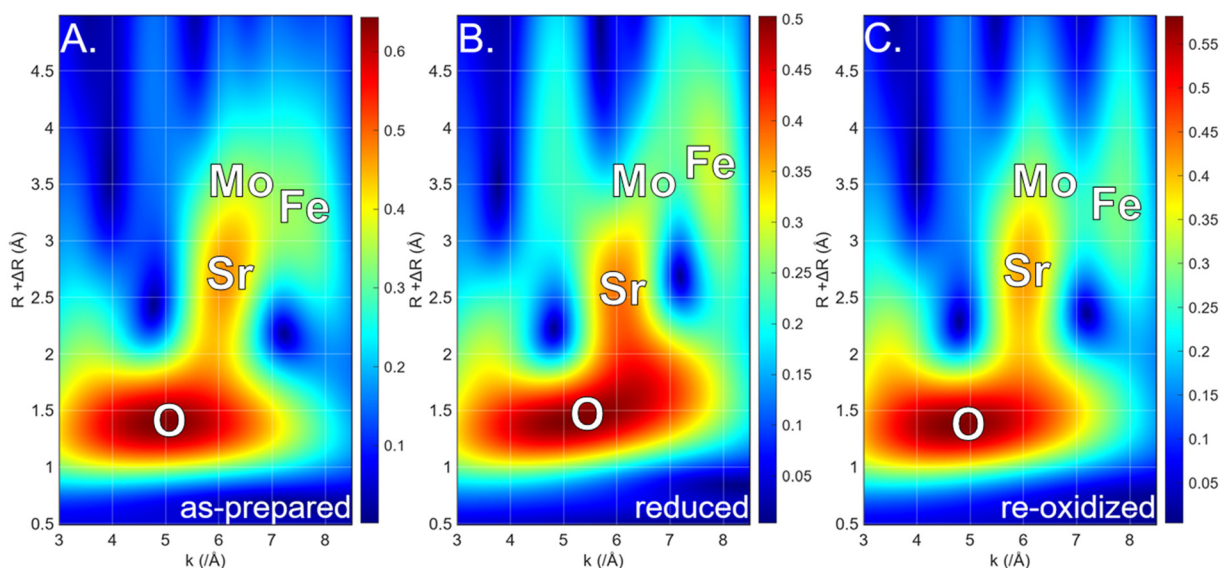


Fig. 8 EXAFS wavelet transform of LSM in the as-prepared (A), reduced (B), and re-oxidized (C) states.



the possible changes during reduction and re-oxidation. The wavelet transform heat maps (not corrected for the phase shift) for the LSFM compound in three states are presented in Fig. 8. The area with the highest intensity, visible as red, is characteristic of the Fe–O bonds, while the longer bond at a wavevector of  $6 \text{ \AA}^{-1}$  originates from interaction with strontium. Both the Fe–O and Fe–Sr bonds are well characterized and are in agreement with the results of Fourier transform EXAFS. At longer radial distances, two halos formed and allowed for distinguishing between iron and molybdenum contributions.<sup>45</sup> It was determined that the halo at approximately  $6 \text{ \AA}^{-1}$  would originate from the Fe–Fe bond,<sup>46,47</sup> while the one at  $7.5 \text{ \AA}^{-1}$  would stand for the Fe–Mo bonds, as heavier atoms should contribute to the signal at higher wavevectors.<sup>48</sup> Both bonds with iron and molybdenum are affected by the reduction and re-oxidation processes; however, the one from molybdenum undergoes more visible elongation and shortens due to the redox processes. Interestingly, an additional signal formed in

the reduced LSFM at a wavevector of  $\sim 4.75 \text{ \AA}^{-1}$ . Despite the same calculation parameters, it is not visible for the as-prepared and re-oxidized states, suggesting that it would be linked to the exsolved particles on the perovskite surface.

### 3.4. Electrical properties

In order to examine the impact of La- and Nb-doping on the electrical properties, the direct current 4-wire method was used. The results of conductivity vs. temperature are plotted in Fig. 9. The three samples in air are characterized by the local maximum of conductivity at 600–650 °C equal to  $14.52 \text{ S cm}^{-1}$ ,  $20.20 \text{ S cm}^{-1}$ , and  $11.03 \text{ S cm}^{-1}$  for SFM, LSFM, and SFMNb, respectively. Below the temperature at which the maximum is achieved, all of the compounds are characterized by thermally activated conduction. The conductivity starts to decrease at a temperature of above 650 °C. Other groups have observed a similar trend.<sup>5,6,10,17,49,50</sup> This behavior is explained by the loss of oxygen from the lattice, which promotes the reduction of

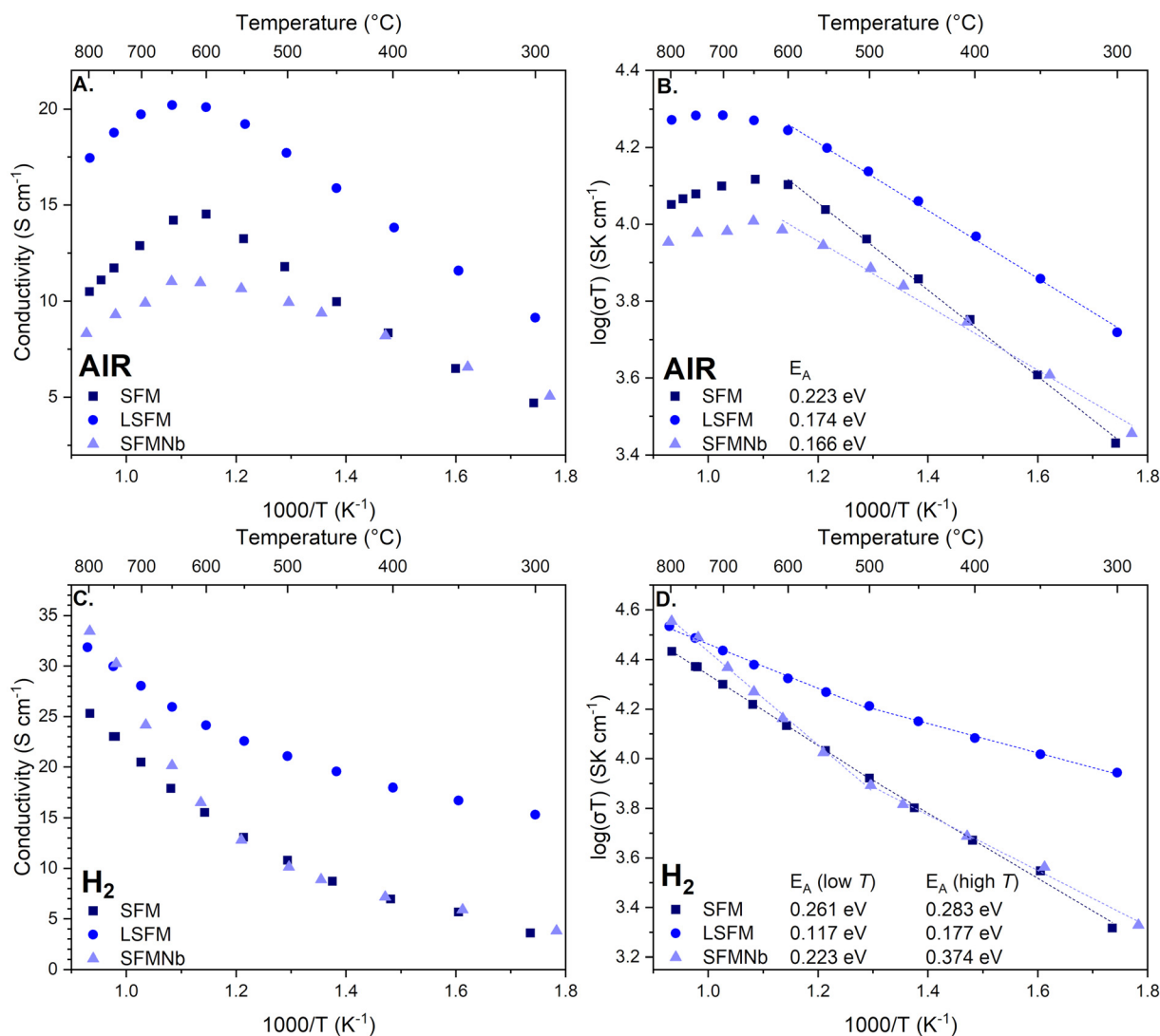


Fig. 9 Electrical conductivities measured in air (A and B) and in hydrogen (C and D).



iron and/or molybdenum, leading to a decrease in the effective charge carrier concentration.<sup>5</sup> At the same time, the formation of oxygen vacancies at higher temperatures would reduce the number of pathways available for the conduction mechanism.<sup>15</sup> According to Niu *et al.*<sup>51</sup> and Yang *et al.*,<sup>6</sup> the conduction in the SFM-based compounds can be explained as double exchange between the Fe 3d–O 2p and Mo 3d–O 2p orbitals. As a result, conduction occurs *via* the small polaron hopping mechanism through the  $\text{Fe}^{2+}/\text{Mo}^{6+}-\text{O}^{2-}-\text{Fe}^{3+}/\text{Mo}^{5+}$  pathway.<sup>6,29,50,52</sup>

As hoped, lanthanum doping has increased the electrical conductivity, but the addition of niobium resulted in lower overall conductivity. At low temperatures, the conductivity of SFMNb is slightly higher than that of the pristine compound. The activation energies were calculated from the Arrhenius formula in the 300–600 °C range, in which  $\ln(\sigma T)$  *vs.*  $1/T$  is characterized by the linear behavior. The calculated  $E_A$  values for both atmospheres are presented in Table 2. In general, the doping process decreased the activation energy of the conductivity. This decrease could be explained by the increased content of oxygen vacancies.<sup>52</sup> Even the Nb-doped sample, regardless of its negative impact on the conduction, is also characterized by a decrease in  $E_A$ .

The conductivity of all compounds in hydrogen has a different behavior; the conductivity gradually increases with temperature throughout the whole temperature range, which is in line with the general behavior.<sup>5,6</sup> Within the conductivity plots, two regions can be differentiated: the low-temperature regime up to 500 °C and the high-temperature region located above this threshold value. Different regimes correspond to the change in the slope of the conductivity curve. The change is the most prominent for the Nb-doped SFM. The presence of the inflection point in the conductivity curve is a characteristic feature of the small polaron hopping mechanism.<sup>50</sup> Wang *et al.*<sup>52</sup> has explained the presence of two slopes by the existence of two different paths of charge compensation. As a result, two different activation energies must be considered. The calculated values are presented in Table 2. In general, the activation energies are lower in the low-temperature regime. Between 300 and 500 °C, doping has a positive impact on the activation energy. However, when the high-temperature region is reached, only lanthanum doping is beneficial in terms of activation energy. Similarly to the behavior in air, LSFM has the highest conductivity in almost the entire temperature range. Only at 800 °C, SFMNb shows the highest electrical conductivity, whereas at lower temperatures, its performance is

comparable to that of undoped SFM. All compounds achieved conductivity values at 800 °C equal to 25.52 S cm<sup>−1</sup>, 31.44 S cm<sup>−1</sup>, and 34.13 S cm<sup>−1</sup> for SFM, LSFM, and SFMNb, respectively. The values obtained for air and hydrogen make those double perovskites promising materials for both the anode and cathode in SOCs and, as a result, could possibly be used as electrodes in symmetrical solid oxide fuel cells (sSOFCs).<sup>19</sup> For example, Zheng *et al.*<sup>53</sup> studied a similar system,  $\text{Sr}_2\text{Fe}_{2-x}\text{W}_x\text{O}_{6-\delta}$ , with an electrical conductivity of  $\sim 40$  S cm<sup>−1</sup> as an electrode in a quasi-symmetrical setup. The same team has also reported the use of SFM in a symmetrical setup with an electrical conductivity of 50 S cm<sup>−1</sup> in an H<sub>2</sub>/Ar mixture and 13 S cm<sup>−1</sup> in air.<sup>21</sup> A similar magnitude of  $\sigma$  was achieved for Cu-doped SFM for use in sSOFCs by Tian *et al.*<sup>17</sup> In the work of Niu *et al.*,<sup>51</sup> good electrode performance, stability, and resistance to poisoning were described for  $\text{Sr}_2\text{TiFe}_{1-x}\text{Mo}_x\text{O}_{6-\delta}$  symmetrical electrodes, even if the electrical conductivity in both air and hydrogen did not exceed 2 S cm<sup>−1</sup>. In light of the aforementioned values, LSFM is undoubtedly worth considering for further studies as an electrode in sSOFCs.

## 4. Conclusions

In this work, it was possible to successfully synthesize a double perovskite  $\text{Sr}_2\text{Fe}_{1.5}\text{Mo}_{0.5}\text{O}_{6-\delta}$  (SFM) and its counterparts doped with La and Nb (LSFM and SFMNb, respectively). Although under highly reducing atmospheres all three compounds undergo a transition to the Ruddlesden–Popper layered perovskite, La-doping stabilizes the structure, and a less new phase was formed. At the same time, exsolution of the Fe-based nanoparticles was observed after the reduction. Moreover, the transition was found to be reversible and the double perovskite structure could be restored after the re-oxidation. *In situ* oxidation studies allowed us to determine that the double perovskite starts with the dissolution of the exsolved iron nanoparticles back into the perovskite base at  $\sim 250$  °C, followed by the incorporation of oxygen up to  $\sim 650$ – $700$  °C. In the *ex situ* XAS measurement, it was found that not only the crystallographic structure is restored to its original but also the local atomic environment can be brought back. As expected, during the reduction, both iron and molybdenum are partially reduced to a lower valence state. The use of wavelet transform on the Fe K-edge enabled us to distinguish between the contributions of Fe–Fe and Fe–Mo bonds in the *k*-space. It is also presented that the Fe–Mo bonds are more prone to elongation and shortening during the redox processes.

Electrical tests performed in both air and hydrogen proved the good electrical conductivity of the SFM-based materials under both atmospheres. The most beneficial was the addition of lanthanum as it almost doubled the conductivity in air when compared with the pristine sample. LSFM also showed the best conductivity in hydrogen. Taking into account the improvement in conductivity and strongly enhanced stability under reducing atmospheres, the LSFM compound seems to be a promising material for sSOFCs.

**Table 2** Activation energies calculated from the Arrhenius formula for the compounds analyzed in air and hydrogen

	AIR	H <sub>2</sub>	
	300–550 °C	300–500 °C	500–800 °C
SFM	0.223(4) eV	0.261(9) eV	0.283(1) eV
LSFM	0.174(4) eV	0.117(4) eV	0.177(5) eV
SFMNb	0.166(7) eV	0.223(9) eV	0.374(9) eV



## Abbreviations and notation

10Dq	Crystal field splitting parameter (eV)
DC4W	Direct current 4-wire method for electrical measurements
DOS	Density of states
DSC	Differential scanning calorimetry
$E_A$	Activation energy (eV)
EXAFS	Extended X-ray absorption fine structure
HT-XRD	High temperature X-ray diffraction
LSFM	$\text{La}_{0.3}\text{Sr}_{1.7}\text{Fe}_{1.5}\text{Mo}_{0.5}\text{O}_{6-\delta}$
Ni-YSZ	Nickel cermet – composite of Ni and YSZ
NPs	Nanoparticles
RP	Ruddlesden–Popper (phase)
SEM	Scanning electron microscopy
SFM	$\text{Sr}_2\text{Fe}_{1.5}\text{Mo}_{0.5}\text{O}_{6-\delta}$
SFMNb	$\text{Sr}_2\text{Fe}_{1.425}\text{Mo}_{0.475}\text{Nb}_{0.1}\text{O}_{6-\delta}$
SOC	Solid oxide cell
SOFC	Solid oxide fuel cell
sSOFC	Symmetrical solid oxide fuel cell
TEY	Total electron yield
TPB	Triple phase boundary
TG	Thermogravimetry
YSZ	Yttria stabilized zirconia
XANES	X-ray absorption near-edge spectroscopy
XAS	X-ray absorption spectroscopy
XRD	X-ray diffraction
$\sigma$	Electrical conductivity ( $\text{S cm}^{-1}$ )

## Author contributions

A. Duka: conceptualization, data curation, formal analysis, investigation, visualization, writing – original draft, writing – review & editing, funding acquisition, and project administration; P. Błaszczak: conceptualization, investigation, writing – original draft, and writing – review & editing; M. Zając: resources and methodology; A. Maximenko: resources, methodology, supervision, and writing – original draft; M. Gazda: resources, methodology, and writing – original draft; B. Bochentyn: resources, investigation, and supervision.

## Data availability

The dataset linked with this manuscript is uploaded and available at the Bridge of Knowledge Repository of Gdańsk University of Technology. The dataset contains all of the techniques used in the manuscript and the prepared figures. The data are sorted accordingly to the methods used.

## Conflicts of interest

The authors declare that they have no known conflict of interest.

## Acknowledgements

This research project was supported by the National Science Center under grant no. NCN 2022/45/N/ST5/02933. This publication was partially developed under the provision of the Polish Ministry and Higher Education project “Support for research and development with the use of research infrastructure of the National Synchrotron Radiation Centre SOLARIS” under contract no 1/SOL/2021/2. We acknowledge the SOLARIS Centre for the access to the PIRX and ASTRA beamlines, where the measurements were performed.

## References

- 1 S. Vasala and M. Karppinen,  $\text{A}_2\text{B}'\text{B}''\text{O}_6$  perovskites: A review, *Prog. Solid State Chem.*, 2015, **43**, 1–36, DOI: [10.1016/j.progsolidstchem.2014.08.001](https://doi.org/10.1016/j.progsolidstchem.2014.08.001).
- 2 X. Xu, Y. Zhong and Z. Shao, Double Perovskites in Catalysis, Electrocatalysis, and Photo(electro)catalysis, *Trends Chem.*, 2019, **1**, 410–424, DOI: [10.1016/j.trechm.2019.05.006](https://doi.org/10.1016/j.trechm.2019.05.006).
- 3 Y. Li, X. Chen, Y. Yang, Y. Jiang and C. Xia, Mixed-Conductor  $\text{Sr}_2\text{Fe}_{1.5}\text{Mo}_{0.5}\text{O}_{6-\delta}$  as Robust Fuel Electrode for Pure  $\text{CO}_2$  Reduction in Solid Oxide Electrolysis Cell, *ACS Nano*, 2017, **5**, 11403–11412, DOI: [10.1021/acsnuschemeng.7b02511](https://doi.org/10.1021/acsnuschemeng.7b02511).
- 4 H. Dong, M. Wang, Y. Liu and Z. Han, Optimized Solid-State Synthesis of  $\text{Sr}_2\text{Fe}_{1.5}\text{Mo}_{0.5}\text{O}_{6-\delta}$  Perovskite: Implications for Efficient Synthesis of Mo-Containing SOFC Electrodes, *Crystals*, 2022, **12**, 1533, DOI: [10.3390/cryst12111533](https://doi.org/10.3390/cryst12111533).
- 5 M. Gou, R. Ren, W. Sun, C. Xu, X. Meng, Z. Wang, J. Qiao and K. Sun, Nb-doped  $\text{Sr}_2\text{Fe}_{1.5}\text{Mo}_{0.5}\text{O}_{6-\delta}$  electrode with enhanced stability and electrochemical performance for symmetrical solid oxide fuel cells, *Ceram. Int.*, 2019, **45**, 15696–15704, DOI: [10.1016/j.ceramint.2019.03.130](https://doi.org/10.1016/j.ceramint.2019.03.130).
- 6 X. Yang, J. Chen, D. Panthi, B. Niu, L. Lei, Z. Yuan, Y. Du, Y. Li, F. Chen and T. He, Electron doping of  $\text{Sr}_2\text{FeMoO}_{6-\delta}$  as high performance anode materials for solid oxide fuel cells, *J. Mater. Chem. A*, 2019, **7**, 733–743, DOI: [10.1039/c8ta10061f](https://doi.org/10.1039/c8ta10061f).
- 7 Q. Liu, C. Yang, X. Dong and F. Chen, Perovskite  $\text{Sr}_2\text{Fe}_{1.5}\text{Mo}_{0.5}\text{O}_6$  as electrode materials for symmetrical solid oxide electrolysis cells, *Int. J. Hydrogen Energy*, 2010, **35**, 10039–10044, DOI: [10.1016/j.ijhydene.2010.08.016](https://doi.org/10.1016/j.ijhydene.2010.08.016).
- 8 Z. Du, H. Zhao, S. Yi, Q. Xia, Y. Gong, Y. Zhang, X. Cheng, Y. Li, L. Gu and K. Świerczek, High-Performance Anode Material  $\text{Sr}_2\text{FeMo}_{0.65}\text{Ni}_{0.35}\text{O}_{6-\delta}$  with In Situ Exsolved Nanoparticle Catalyst, *ACS Nano*, 2016, **10**(9), 8660–8669, DOI: [10.1021/acsnano.6b03979](https://doi.org/10.1021/acsnano.6b03979).
- 9 Y. Li, M. Singh, Z. Zhuang, Y. Jing, F. Li and K. Maliutina, Efficient reversible  $\text{CO}/\text{CO}_2$  conversion in solid oxide cells with a phase-transformed fuel electrode, *Sci. China Mater.*, 2021, **64**, 1114–1126, DOI: [10.1007/s40843-020-1531-7](https://doi.org/10.1007/s40843-020-1531-7).
- 10 Y. Wu, H. Li, P. Zhang, S. Tong, X. Han, H. Chen, B. Wei and Z. Lü, Multiphase engineering regulation of double per-





- ovskite and RP structure heterojunction interfaces for solid oxide fuel cells, *Sustainable Mater. Technol.*, 2024, **40**(e00905), DOI: [10.1016/j.susmat.2024.e00905](https://doi.org/10.1016/j.susmat.2024.e00905).
- 11 Y. Yang, W. Li, S. Yang, X. Shen, Z. Han, H. Yu, M. Gao, K. Wang and Z. Yang, Ni-Substituted  $\text{Sr}_2\text{FeMoO}_{6-\delta}$  as an Electrode Material for Symmetrical and Reversible Solid-Oxide Cells, *ACS Appl. Mater. Interfaces*, 2024, **16**, 21790–21798, DOI: [10.1021/acsami.4c00509](https://doi.org/10.1021/acsami.4c00509).
  - 12 H. Lv, L. Lin, X. Zhang, Y. Song, H. Matsumoto, C. Zeng, N. Ta, W. Liu, D. Gao, G. Wang and X. Bao, In Situ Investigation of Reversible Exsolution/Dissolution of CoFe Alloy Nanoparticles in a Co-Doped  $\text{Sr}_2\text{Fe}_{1.5}\text{Mo}_{0.5}\text{O}_{6-\delta}$  Cathode for  $\text{CO}_2$  Electrolysis, *Adv. Mater.*, 2020, **32**, 1906193, DOI: [10.1002/ADMA.201906193](https://doi.org/10.1002/ADMA.201906193).
  - 13 P. Qiu, X. Yang, W. Wang, T. Wei, Y. Lu, J. Lin, Z. Yuan, L. Jia, J. Li and F. Chen, Redox-Reversible Electrode Material for Direct Hydrocarbon Solid Oxide Fuel Cells, *ACS Appl. Mater. Interfaces*, 2020, **12**, 13988–13995, DOI: [10.1021/acsami.0c00922](https://doi.org/10.1021/acsami.0c00922).
  - 14 Y. Luo, X. Chang, J. Wang, D. Zhang, L. Fu, X. K. Gu, *et al.*, Precise Regulation of In Situ Exsolution Components of Nanoparticles for Constructing Active Interfaces toward Carbon Dioxide Reduction, *ACS Nano*, 2025, **19**, 1463–1477, DOI: [10.1021/acs.nano.4c14279](https://doi.org/10.1021/acs.nano.4c14279).
  - 15 P. Shan, H. Ye, B. Qian, Y. Zheng and G. Xiao, Boosting the catalytic activity of high-order Ruddlesden–Popper perovskite  $\text{SrEu}_2\text{Fe}_2\text{O}_{7-\delta}$  air electrode by A-site La doping for  $\text{CO}_2$  electrolysis in solid oxide electrolysis cells, *Fuel*, 2024, **367**, 131507, DOI: [10.1016/j.fuel.2024.131507](https://doi.org/10.1016/j.fuel.2024.131507).
  - 16 K. Zhu, B. Luo, Z. Liu and X. Wen, Recent advances and prospects of symmetrical solid oxide fuel cells, *Ceram. Int.*, 2022, **48**, 8972–8986, DOI: [10.1016/j.ceramint.2022.01.258](https://doi.org/10.1016/j.ceramint.2022.01.258).
  - 17 C. Tian, J. Cheng and J. Yang, A highly active cathode material of Cu-doped  $\text{Sr}_2\text{Fe}_{1.5}\text{Mo}_{0.5}\text{O}_6$  for symmetrical solid oxide fuel cells, *J. Mater. Sci.: Mater. Electron.*, 2021, **32**, 1258–1264, DOI: [10.1007/s10854-020-04898-z](https://doi.org/10.1007/s10854-020-04898-z).
  - 18 Q. Liu, X. Dong, G. Xiao, F. Zhao and F. Chen, A novel electrode material for symmetrical SOFCs, *Adv. Mater.*, 2010, **22**, 5478–5482, DOI: [10.1002/adma.201001044](https://doi.org/10.1002/adma.201001044).
  - 19 J. C. Ruiz-Morales, D. Marrero-López, J. Canales-Vázquez and J. T. S. Irvine, Symmetric and reversible solid oxide fuel cells, *RSC Adv.*, 2011, **1**, 1403–1414, DOI: [10.1039/c1ra00284h](https://doi.org/10.1039/c1ra00284h).
  - 20 B. He, L. Zhao, S. Song, T. Liu, F. Chen and C. Xia,  $\text{Sr}_2\text{Fe}_{1.5}\text{Mo}_{0.5}\text{O}_{6-\delta}$  -  $\text{Sm}_{0.2}\text{Ce}_{0.8}\text{O}_{1.9}$  Composite Anodes for Composite Anodes for Intermediate-Temperature Solid Oxide Fuel Cells Intermediate-Temperature Solid Oxide Fuel Cells, *J. Electrochem. Soc.*, 2012, **159**, 619–626, DOI: [10.1149/2.020206jes](https://doi.org/10.1149/2.020206jes).
  - 21 K. Zheng, K. Świerczek, J. M. Polfus, M. F. Sunding, M. Pishahang and T. Norby, Carbon Deposition and Sulfur Poisoning in  $\text{SrFe}_{0.75}\text{Mo}_{0.25}\text{O}_{3-\delta}$  and  $\text{SrFe}_{0.5}\text{Mn}_{0.25}\text{Mo}_{0.25}\text{O}_{3-\delta}$  Electrode Materials for Symmetrical SOFCs, *J. Electrochem. Soc.*, 2015, **162**, 1078–1087, DOI: [10.1149/2.0981509jes](https://doi.org/10.1149/2.0981509jes).
  - 22 Y. Wang, T. Liu, S. Fang and F. Chen, Syngas production on a symmetrical solid oxide  $\text{H}_2\text{O}/\text{CO}_2$  co-electrolysis cell with  $\text{Sr}_2\text{Fe}_{1.5}\text{Mo}_{0.5}\text{O}_6$ - $\text{Sm}_{0.2}\text{Ce}_{0.8}\text{O}_{1.9}$  electrodes, *J. Power Sources*, 2016, **305**, 240–248, DOI: [10.1016/j.jpowsour.2015.11.097](https://doi.org/10.1016/j.jpowsour.2015.11.097).
  - 23 Y. Huan, Y. Li, B. Yin, D. Ding and T. Wei, High conductive and long-term phase stable anode materials for SOFCs:  $\text{A}_2\text{FeMoO}_6$  (A = Ca, Sr, Ba), *J. Power Sources*, 2017, **359**, 384–390, DOI: [10.1016/j.jpowsour.2017.05.079](https://doi.org/10.1016/j.jpowsour.2017.05.079).
  - 24 X. Li, H. Zhao, N. Xu, X. Zhou, C. Zhang and N. Chen, Electrical conduction behavior of La, Co co-doped  $\text{SrTiO}_3$  perovskite as anode material for solid oxide fuel cells, *Int. J. Hydrogen Energy*, 2009, **34**, 6407–6414, DOI: [10.1016/j.ijhydene.2009.05.079](https://doi.org/10.1016/j.ijhydene.2009.05.079).
  - 25 S. Vasala, M. Lehtimäki, S. C. Haw, J. M. Chen, R. S. Liu, H. Yamauchi and M. Karppinen, Isovalent and aliovalent substitution effects on redox chemistry of  $\text{Sr}_2\text{MgMoO}_{6-\delta}$  SOFC-anode material, *Solid State Ionics*, 2010, **181**, 754–759, DOI: [10.1016/j.ssi.2010.03.037](https://doi.org/10.1016/j.ssi.2010.03.037).
  - 26 X. Hu, J. Qi, X. Fu, J. Liu, S. Qiao, Y. Gao, R. Zhao, J. Shang, L. Liu, L. Tang and W. Zhang, Conductive origin and design principles of electrically controllable high conductivity La-doped perovskites, *J. Mater. Chem. A*, 2024, **12**, 4019–4028, DOI: [10.1039/d3ta06845e](https://doi.org/10.1039/d3ta06845e).
  - 27 R. D. Shannon, Revised effective ionic radii and systematic studies of interatomic distances in halides and chalcogenides, *Acta Crystallogr.*, 1976, **32**, 751–767, DOI: [10.1107/s0567739476001551](https://doi.org/10.1107/s0567739476001551).
  - 28 N. Yu, T. Liu, X. Chen, M. Miao, M. Ni and Y. Wang, Co-generation of liquid chemicals and electricity over Co-Fe alloy/perovskite anode catalyst in a propane fueled solid oxide fuel cell, *Sep. Purif. Technol.*, 2022, **291**, 120890, DOI: [10.1016/j.seppur.2022.120890](https://doi.org/10.1016/j.seppur.2022.120890).
  - 29 X. Xi, Z. S. Cao, X. Q. Shen, Y. Lu, J. Li, J. L. Luo and X. Z. Fu, In situ embedding of CoFe nanocatalysts into  $\text{Sr}_3\text{FeMoO}_7$  matrix as high-performance anode materials for solid oxide fuel cells, *J. Power Sources*, 2020, **459**, 228071, DOI: [10.1016/j.jpowsour.2020.228071](https://doi.org/10.1016/j.jpowsour.2020.228071).
  - 30 A. Awasthi, Y. J. Bhatt, N. Krishnamurthy, Y. Ueda and S. P. Garg, The reduction of niobium and tantalum pentoxides by silicon in vacuum, *J. Alloys Compd.*, 2001, **315**(1–2), 187–192, DOI: [10.1016/S0925-8388\(00\)01274-3](https://doi.org/10.1016/S0925-8388(00)01274-3).
  - 31 J. Suntivich, W. T. Hong, Y. L. Lee, J. M. Rondinelli, W. Yang, J. B. Goodenough, B. Dabrowski, J. W. Freeland and Y. Shao-Horn, Estimating Hybridization of Transition Metal and Oxygen States in Perovskites from O K-edge X-ray Absorption Spectroscopy, *J. Phys. Chem. C*, 2014, **118**, 1856–1863, DOI: [10.1021/jp410644j](https://doi.org/10.1021/jp410644j).
  - 32 M. Abbate, F. M. F. De Groot, J. C. Fuggle, A. Fujimori, O. Strebel, M. F. Lopez, M. Domke, G. Kaindl, G. Sawatzky, M. Takano, Y. Takeda, H. Eisaki and S. Uchida, Controlled-Valence Properties of  $\text{La}_{1+x}\text{Sr}_x\text{FeO}_3$  and  $\text{La}_{1+x}\text{Sr}_x\text{MnO}_3$  Studied by Soft-X-ray Absorption Spectroscopy, *Phys. Rev. B: Condens. Matter*, 1992, **46**, 4511–4519, DOI: [10.1103/PhysRevB.46.4511](https://doi.org/10.1103/PhysRevB.46.4511).
  - 33 Z. Wu, M. Benfatto, M. Pedio, R. Cimino, S. Mobilio, S. R. Barman, K. Maiti and D. D. Sarma, Theoretical ana-



- lysis of x-ray-absorption near-edge fine structure at the O and metal K edges of  $\text{LaFeO}_3$  and  $\text{LaCoO}_3$ , *Phys. Rev. B: Condens. Matter*, 1997, **56**, 2228–2233, DOI: [10.1103/PhysRevB.56.2228](#).
- 34 F. Frati, M. O. J. Y. Hunault and F. M. F. De Groot, Oxygen K-edge X-ray Absorption Spectra, *Chem. Rev.*, 2020, **120**, 4056–4110, DOI: [10.1021/acs.chemrev.9b00439](#).
  - 35 X. A. Xi, J. W. Liu, W. Z. Luo, Y. Fan, J. J. Zhang, J.-L. Luo and X.-Z. Fu, Unraveling the Enhanced Kinetics of  $\text{Sr}_2\text{Fe}_{1+x}\text{Mo}_{1-x}\text{O}_{6-\delta}$  Electrocatalysts for High-Performance Solid Oxide Cells, *Adv. Energy Mater.*, 2021, **11**, 2102845, DOI: [10.1002/aenm.202102845](#).
  - 36 Y. Liao, X. Xi, H. Chen, J. Liu, X. Z. Fu and J. L. Luo, The emerging  $\text{Sr}_2\text{FeMoO}_6$ -based electrocatalysts for solid oxide electrochemical cell: synthesis, modulation and applications, *Chem. Synth.*, 2024, **4**(18), DOI: [10.20517/cs.2023.47](#).
  - 37 H. Sun, X. Xu, Z. Hu, L. H. Tjeng, J. Zhao, Q. Zhang, H.-J. Lin, C.-T. Chen, T.-S. Chan, W. Zhou and Z. Shao, Boosting the oxygen evolution reaction activity of a perovskite through introducing multi-element synergy and building an ordered structure, *J. Mater. Chem. A*, 2019, **7**, 9924–9932, DOI: [10.1039/c9ta01404g](#).
  - 38 P. Kuiper, B. G. Searle, P. Rudolf, L. H. Tjeng and C. T. Chen, X-ray magnetic dichroism of antiferromagnet  $\text{Fe}_2\text{O}_3$ : The orientation of magnetic moments observed by Fe 2p X-ray absorption spectroscopy, *Phys. Rev. Lett.*, 1993, **70**, 1549–1552, DOI: [10.1103/PhysRevLett.70.1549](#).
  - 39 C. Y. Kuo, Z. Hu, J. C. Yang, S. C. Liao, Y. L. Huang, R. K. Vasudevan, M. B. Okatan, S. Jesse, S. V. Kalinin, L. Li, H. J. Liu, C.-H. Lai, T. W. Pi, S. Agrestini, K. Chen, P. Ohresser, A. Tanaka, L. H. Tjeng and Y. H. Chu, Single-domain multiferroic  $\text{BiFeO}_3$  films, *Nat. Commun.*, 2016, **7**, 1–7, DOI: [10.1038/ncomms12712](#).
  - 40 M. L. Baker, M. W. Mara, J. J. Yan, K. O. Hodgson, B. Hedman and E. I. Solomon, K- and, L-edge X-ray absorption spectroscopy (XAS) and resonant inelastic X-ray scattering (RIXS) determination of differential orbital covalency (DOC) of transition metal sites, *Coord. Chem. Rev.*, 2017, **345**, 182–208, DOI: [10.1016/j.ccr.2017.02.004](#).
  - 41 T. E. Westre, P. Kennepohl, J. G. DeWitt, B. Hedman, K. O. Hodgson and E. I. Solomon, A multiplet analysis of Fe K-edge  $1s \rightarrow 3d$  pre-Edge features of iron complexes, *J. Am. Chem. Soc.*, 1997, **119**, 6297–6314, DOI: [10.1021/ja964352a](#).
  - 42 T. Yamamoto, Assignment of pre-edge peaks in K-edge X-ray absorption spectra of 3d transition metal compounds: electric dipole or quadrupole?, *X-Ray Spectrom.*, 2008, **37**, 572–584, DOI: [10.1002/xrs.1103](#).
  - 43 A. P. Freitas, R. F. André, C. Poucin, T. K. C. Le, J. Imbao, B. Lassalle-Kaiser and S. Carenco, Guidelines for the Molybdenum Oxidation State and Geometry from X-ray Absorption Spectroscopy at the Mo  $L_{2,3}$ -Edges, *J. Phys. Chem. C*, 2021, **125**, 17761–17773, DOI: [10.1021/acs.jpcc.1c01875](#).
  - 44 H. Aritani, T. Tanaka, T. Funabiki, S. Yoshida, K. Eda, N. Sotani, M. Kudo and S. Hasegawa, Study of the local structure of molybdenum-magnesium binary oxides by means of Mo  $L_3$ -edge XANES and UV-vis spectroscopy, *J. Phys. Chem.*, 1996, **100**, 19495–19501, DOI: [10.1021/jp9615464](#).
  - 45 A. Iglesias-Juez, G. L. Chiarello, G. S. Patience and M. O. Guerrero-Pérez, Experimental methods in chemical engineering: X-ray absorption spectroscopy—XAS, XANES, EXAFS, *Can. J. Chem. Eng.*, 2022, **100**, 3–22, DOI: [10.1002/cjce.24291](#).
  - 46 D. Li, H. Li, Q. Wen, C. Gao, F. Song and J. Zhou, Investigation on Photo-Assisted Fenton-like Mechanism of Single-Atom Mn–N–Fe–N–Ni Charge Transfer Bridge Across Six-Membered Cavity of Graphitic Carbon Nitride, *Adv. Funct. Mater.*, 2024, **34**, 1–14, DOI: [10.1002/adfm.202313631](#).
  - 47 L. Zhu, Z. Li, M. Yang, Y. Zhou, J. Chen, F. Xie, N. Wang, Y. Jin, S. Sun and H. Meng, An Effective Approach to Enhance Hydrogen Evolution Reaction and Hydrogen Oxidation Reaction by Ni Doping to  $\text{MoO}_3$ , *Small*, 2023, **19**, 1–8, DOI: [10.1002/sml.202303481](#).
  - 48 M. Muñoz, F. Farges and P. Argoul, Continuous Cauchy wavelet transform of XAFS spectra, *Phys. Scr.*, 2005, **T115**, 221–222, DOI: [10.1238/Physica.Topical.115a00221](#).
  - 49 L. Chen, J. Xu, X. Wang and K. Xie,  $\text{Sr}_2\text{Fe}_{1.5+x}\text{Mo}_{0.5}\text{O}_6$  cathode with exsolved Fe nanoparticles for enhanced  $\text{CO}_2$  electrolysis, *Int. J. Hydrogen Energy*, 2020, **45**, 2–8, DOI: [10.1016/j.ijhydene.2020.02.140](#).
  - 50 M. K. Rath and K. T. Lee, Superior electrochemical performance of non-precious Co–Ni–Mo alloy catalyst-impregnated  $\text{Sr}_2\text{FeMoO}_{6-\delta}$  as an electrode material for symmetric solid oxide fuel cells, *Electrochim. Acta*, 2016, **212**, 678–685, DOI: [10.1016/j.electacta.2016.07.037](#).
  - 51 B. Niu, F. Jin, L. Zhang, P. Shen and T. He, Performance of double perovskite symmetrical electrode materials  $\text{Sr}_2\text{TiFe}_{1-x}\text{Mo}_x\text{O}_{6-\delta}$  ( $x = 0.1, 0.2$ ) for solid oxide fuel cells, *Electrochim. Acta*, 2018, **263**, 217–227, DOI: [10.1016/J.ELECTACTA.2018.01.062](#).
  - 52 Y. Wang, X. Lei, Y. Zhang, F. Chen and T. Liu, In-situ growth of metallic nanoparticles on perovskite parent as a hydrogen electrode for solid oxide cells, *J. Power Sources*, 2018, **405**, 114–123, DOI: [10.1016/J.JPOWSOUR.2018.10.023](#).
  - 53 K. Zheng, J. Lach, P. Czaja, M. Gogacz, P. Czach, A. Brzozakos, P. Winiarz and J. Luo, Designing high-performance quasi-symmetrical solid oxide cells with a facile chemical modification strategy for  $\text{Sr}_2\text{Fe}_{2-x}\text{W}_x\text{O}_{6-\delta}$  ferrites electrodes with in situ exsolution of nanoparticles, *J. Power Sources*, 2023, **587**, 233707, DOI: [10.1016/j.jpowsour.2023.233707](#).

